Engineering Structures 341 (2025) 120798

Contents lists available at ScienceDirect

Engineering Structures

journal homepage: www.elsevier.com/locate/engstruct

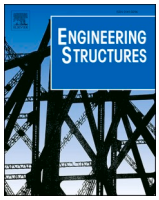

Testing of additively manufactured aluminium material and cross-sections in compression

Ruizhi Zhang [a,*], Mohsen Amraei [b], Heidi Piili [b], Leroy Gardner [a]

[a] Department of Civil and Environmental Engineering, Imperial College London, London, UK
[b] Department of Mechanical Engineering, University of Turku, Turku, Finland

ARTICLE INFO

Keywords:
Additive manufacturing
Aluminium
Material coupon tests
Powder bed fusion
Square hollow sections
Stub column testing
Structural design methods

ABSTRACT

A comprehensive experimental investigation into the mechanical properties and structural performance of square hollow section (SHS) stub columns manufactured by laser beam powder bed fusion (PBF-LB/M) from AlSi10Mg aluminium alloy, has been conducted and is presented herein. A series of tensile and compressive coupons with different build directions, together with six SHS stub columns, were additively manufactured and tested. The PBF-LB/M AlSi10Mg material exhibited good mechanical performance and mild anisotropy, with yield and ultimate strengths of around 280 MPa and 420 MPa, respectively, and fracture strains of between about 4 % and 7 %. SHS profiles were examined to isolate the influence of the manufacturing process, enabling direct comparisons with the performance and design of conventionally produced cross-sections. The PBF-LB/M aluminium SHS stub columns failed by inelastic local buckling and exhibited similar performance to conventionally manufactured aluminium SHS in the slender range, while showing higher normalised load-carrying capacities in the stocky range. Comparisons with the existing design methods indicated that both Eurocode 9 (EC9) and the continuous strength method (CSM) can provide safe-sided resistance predictions, with the CSM yielding more accurate and consistent results.

1. Introduction

Metal additive manufacturing (AM), commonly known as metal 3D printing, is a means of producing 3D metallic components in a repeated layerwise fashion via the deposition, fusion and solidification of feedstock materials at programmed locations [1]. Metal AM has experienced exponential growth in the aerospace, automotive and biomedical sectors over the past few decades, due to its excellent ability to reduce material waste, enhance design flexibility and streamline workflows, contributing to more sustainable and efficient manufacturing practices. The integration of AM in the construction industry has progressed [1–3] but less rapidly than in other sectors, with one key obstacle being the lack of structural design guidance for AM structural elements, underpinned by a robust database of experimental results.

Laser beam powder bed fusion (PBF-LB/M) is a method of metal 3D printing that is suited to producing complex and highly optimised structures with high dimensional accuracy, but generally at slower deposition rates than wire-based AM methods, such as wire arc additive manufacturing (WAAM) [4–6] and wire laser metal deposition [7]. A diverse range of materials can be printed using PBF-LB/M, including aluminium [8], stainless steel [9–11] and titanium [12], among which aluminium alloys are particularly favoured for applications in aerospace and automotive industries due to their high strength-to-weight ratio, thermal conductivity and reflectivity. Numerous studies have focused on the influence of process parameters and post-processing on the defects, microstructure and mechanical properties of aluminium parts manufactured by PBF-LB/M [13–15], and found that PBF-LB/M aluminium parts with suitable process parameters exhibit comparable or higher hardness and strength relative to their conventionally manufactured counterparts [16]. The degree of material anisotropy in AM aluminium alloys has been extensively investigated [17,18] and links to the crystallographic texture, grain morphology and other characteristics such as defects arising from the fabrication process [19,20]. The directional properties can be varied by altering the process parameters, for example the scan strategy, to meet specific engineering requirements for different applications [18]. Other studies into the behaviour of structural elements produced by PBF-LB/M and WAAM carbon steel [21–23] and stainless steel [9–11,24,25] can also be found in the literature.

* Corresponding author.
E-mail addresses: ruizhi.zhang@imperial.ac.uk (R. Zhang), mohsen.amraei@utu.fi (M. Amraei), heidi.piili@utu.fi (H. Piili), leroy.gardner@imperial.ac.uk (L. Gardner).

https://doi.org/10.1016/j.engstruct.2025.120798
Received 18 March 2025; Received in revised form 13 May 2025; Accepted 16 June 2025
Available online 30 June 2025

Considerable effort has been also dedicated to structural optimisation specifically for AM [21,26,27], aiming to fully exploit the unique advantages of AM in producing complex geometries that were previously constrained by the manufacturability limitations imposed by conventional formative and subtractive manufacturing methods.

Despite these advances in AM, there has been a lack of research into the structural behaviour of aluminium elements produced by PBF-LB/M and their suitability for use in construction. This study aims to address this gap by experimentally investigating the material and structural performance of aluminium square hollow section (SHS) stub columns produced by PBF-LB/M, with an emphasis on the mechanical behaviour and the evaluation of current design provisions. SHS stub columns and coupons with different build directions were manufactured using PBF-LB/M from AlSi10Mg powder and tested. The experiments comprised tensile and compressive coupon tests, geometric measurements and six SHS stub column tests, supported by advanced testing techniques – 3D laser scanning and digital image correlation (DIC) [28–30]. The experimental results are analysed and utilised to evaluate the applicability of existing design approaches for conventionally formed plated cross-sections to PBF-LB/M aluminium SHS.

2. Specimen manufacture and preparation

18 tensile coupons, six compressive coupons and six SHS stub columns were built using an SLM 280 HL twin metal printer, featuring a 280 mm × 280 mm × 365 mm building chamber and two Yb-fibre lasers, in the Department of Mechanical and Materials Engineering at the University of Turku. The PBF-LB/M process featured a recoater spreading a layer of metallic powder onto the build plate that was preheated to 150 ℃ and high-energy laser beams selectively melting the powder particles and fused them onto the existing solidified layers at specific locations based on a 3D digital model, until the final completion of target part. The detailed PBF-LB/M processing parameters, including the laser power, the focal point diameter of the laser, the scanning speed, the layer thickness and the hatch distance, were set by SLM Solutions, as provided in Table 1. The specimens were deposited using the bi-directional stripe scanning strategy, with a 67° scan rotation angle between successive layers to reduce residual stresses and distortions in the final parts. Inert argon was used as the shielding gas to prevent oxidation during the manufacturing process.

The adopted feedstock material was AlSi10Mg powder, with its nominal chemical composition shown in Table 2 [31]. The nominal mechanical properties of the employed PBF-LB/M aluminium are listed in Table 3 [31], along with those of the cast alloy EN AC-43000 in the T6 heat treated condition, as provided in [32,33]. The particle size distribution of the aluminium powder was measured using a laser diffraction particle machine (Malvern Mastersizer 2000) in the Centre for Infrastructure Materials of the Department of Civil and Environmental Engineering at Imperial College London; the results are presented in Fig. 1. The average measured particle size was 48.4 μm, with a range of 30–80 μm, in line with the nominal particle size distribution of 20–63 μm, as provided by SLM Solutions [31].

The tensile and compressive coupons were printed at 0°, 45° and 90° relative to the build plate (i.e. θ=0°, 45° and 90°, where θ is the angle between the longitudinal axis of the specimen and the deposition layers), while the stub columns were printed vertically with their longitudinal axes perpendicular to the deposition layers, at a deposition rate of 29.8 cm^3/hour. The positions of the coupons and stub columns are illustrated in Fig. 2, also showing the definition of the coupon orientations. A spacing of approximately 15 mm between parts was used to avoid spatter and any localised overheating and distortion in the PBF-LB/M builds. The nominal dimensions of the tensile and compressive coupons, as determined in accordance with EN ISO 6892–1 [35] and existing studies [47,48], respectively, along with those of the SHS stub columns, are shown in Fig. 3. Support structures were printed to hold specimens in place during the build and to reduce the distortion induced by the removal of the build plate. Upon completion of printing, each specimen was removed from the build plate using a bandsaw, and no additional thermal stress relief or other post-processing was carried out. A photo of all SHS stub columns after detachment from the base plate is shown in Fig. 4. In total, the printed specimens weighed 1.7 kg, but 60 kg of metal powder was needed to fill the building chamber, with the excess powder collected for future prints. The cost of the aluminium powder was approximately £ 50/kg from the original equipment manufacturer [31], compared to £ 2.5/kg of equivalent cast aluminium ingots [34].

The coupon labelling system starts with the letter ‘T’ for tensile coupons or ‘C’ for compressive coupons, followed by the plane in which the coupons were printed, the build orientation angle, as defined in Fig. 2, and finally a number representing the repeated coupons. For instance, coupon T-XZ-0-2 is the second tensile coupon printed in the XZ plane, with its longitudinal axis being at an angle of 0° relative to the build plane. Three repeated tensile coupons and two repeated compressive coupons were tested for each build orientation. In total, 18 dog-bone tensile coupons and six rectangular compressive coupons with different build directions were tested.

3. Tensile and compressive coupon tests

Uniaxial tensile and compressive coupon tests were conducted to determine the mechanical response of the investigated PBF-LB/M aluminium and to examine the possible anisotropy and non-symmetry of stress–strain behaviour in tension and compression in the Structures Laboratory of the Department of Civil and Environmental Engineering at Imperial College London. The description of the test setup and procedure, and detailed analysis of the test results are provided in this section.

3.1. Tensile coupon tests

All tensile coupon tests were conducted using an Instron 8802 250 kN hydraulic testing machine, equipped with hydraulic grips. The testing machine was operated in displacement control in accordance with EN ISO 6892–1 [35], with crosshead separation rates being set to achieve a strain rate of 0.007 % s^{-1} up to the 0.2 % proof strength $\sigma_{0.2}$ and of 0.025 % s^{-1} beyond yielding with a smooth transition between them. Before testing, the width and thickness of the parallel section of the coupons were measured using a digital calliper, and standard gauge lengths equal to $5.65\sqrt{A}$ [35], where A is the average cross-sectional area of the parallel length, were scribed onto the two sides of each coupon for the post-test calculation of the fracture strain ε_f.

The test setup is presented in Fig. 5. A four-camera StrainMaster Compact DIC system, equipped with two cameras featuring 5 MP resolution, a device control unit and an integrated light source for each side, was used to capture the surface deformations and strains along the parallel length on both the front and back faces of each coupon. Prior to testing, the coupon faces were spray-painted with a matte black layer to eliminate reflections, followed by a random pattern of white speckles for their relative movements between sequential images to be tracked.

Table 1
PBF processing parameters adopted in this study.

Laser power (W)	Laser spot diameter (μm)	Scanning speed (mm/s)	Layer thickness (μm)	Hatch distance (μm)	Scanning rotation (°)	Preheated powder bed (℃)	Shielding gas
370	80	1150	30	120	67	150	Argon

Table 2
Nominal chemical composition of the employed AlSi10Mg powder provided by the manufacturer [31] (unit: wt%).

Si	Fe	Cu	Mn	Mg	Ni	Zn	Pb	Sn	Ti	Al
9.0–11.0	< 0.55	< 0.05	< 0.45	0.20–0.45	< 0.05	< 0.10	< 0.05	< 0.05	< 0.15	balance

Table 3
Nominal material properties of parts built using the employed AlSi10Mg powder.

Source	θ (°)	E (kN/mm^2)	$\sigma_{0.2}$ (N/mm^2)	σ_u (N/mm^2)	ε_f (%)
As-built [31]	0	–	305	465	9.0
	90	–	270	475	6.0
EN AC-43000, T6 [32,33]	–	71	165–220	310–328	3.5

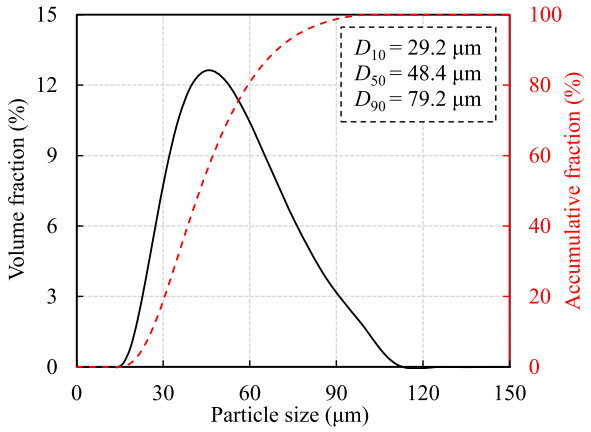

Fig. 1. Measured particle size distribution of the adopted AlSi10Mg powder.

Stereo calibration was performed by detecting a grid of markers on the calibration board to map pixel data to real points for the DIC cameras. The applied load, measured using a load cell within the Instron testing machine, was transmitted to the DIC system via an analogue-to-digital converter (ADC). During testing, the load readings and DIC images were synchronously recorded at 1-second intervals and post-processed using the DaVis 10 software package [36]. A similar test setup and procedure was employed in [37,38].

The engineering stress-strain curves for all coupons are presented in Fig. 6, where the typical value of $E = 70000$ MPa for conventional aluminium [39] is also plotted. The strains were averaged over the full parallel length of both faces of the coupons. A moving average filter with

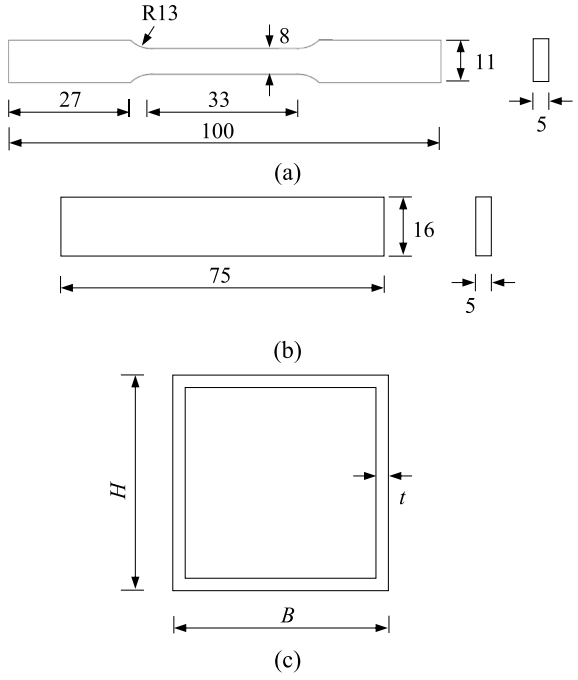

Fig. 3. Dimensions (in mm) and notation of (a) tensile coupons, (b) compressive coupons and (c) SHS stub columns.

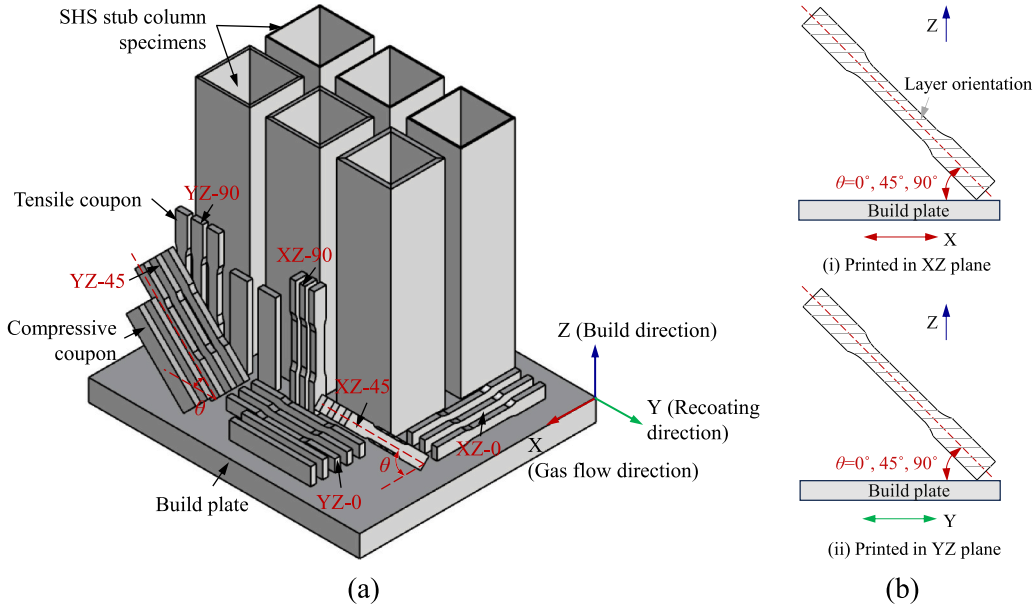

Fig. 2. (a) Schematic illustration of printed coupons and stub columns, (b) coupon orientation angles: (i) printed in YZ plane and (ii) printed in XZ plane.

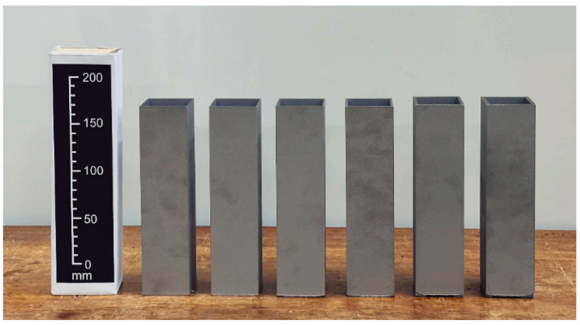

Fig. 4. Printed SHS stub columns, with increasing wall thickness from left to right.

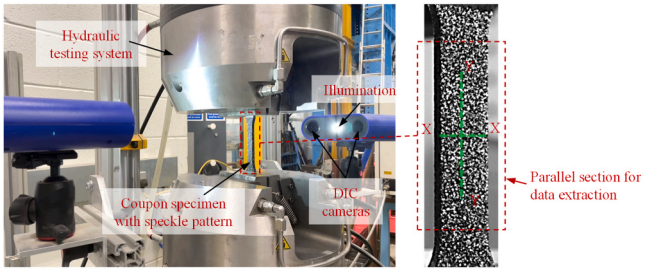

Fig. 5. Setup of tensile coupon tests.

a window of 10 data points was applied to the raw data from the DIC system to reduce the experimental noise. The stress-strain response of the PBF-LB/M aluminium was found to be influenced by the build direction, with the highest strain hardening found in the vertical coupons (θ=90°). Typical transverse and longitudinal stress-strain curves are plotted in Fig. 7. Fig. 8 shows all coupons after fracture. The fracture of all coupons was abrupt with minimal visible necking, and the build direction was found to have a negligible effect on the appearance of the fracture surfaces.

The derived mechanical properties – the Young's modulus E, ν is the Poisson's ratio, 0.2 % proof strength $\sigma_{0.2}$, 1.0 % proof strength $\sigma_{1.0}$, 2.0 % proof strength $\sigma_{2.0}$, ultimate tensile strength σ_u and corresponding strain ε_u, fracture strain over the marked gauge length ε_f and the strain hardening parameters of the two-stage Ramberg-Osgood material model n [40,41], $m_{1.0}$ and m_u [42,43], are summarised in Table 4. Note that the Young's modulus E was calculated as the slope of linear portion of the stress-strain curve, between approximately $0.1\sigma_{0.2}$ and $0.4\sigma_{0.2}$, and the

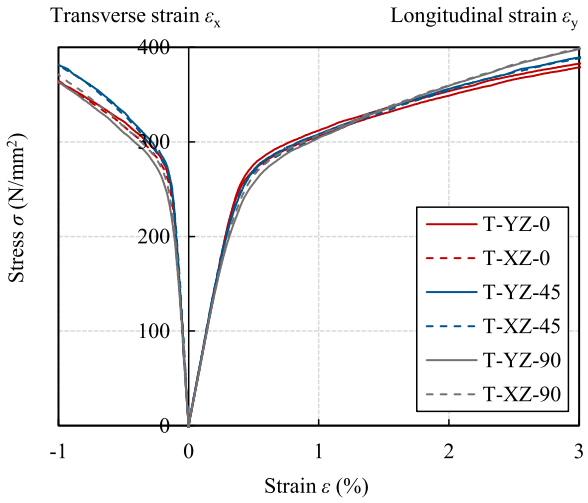

Fig. 7. Typical transverse and longitudinal stress-strain curves from tensile coupon tests.

Poisson's ratio ν was determined as the ratio of the mean transverse to mean longitudinal strains within the same range. The mechanical properties measured in this study are comparable to the values reported by SLM Solutions and significantly higher than those of high pressure die cast AlSi10Mg, as reported in Table 3 [31,32]; this is in consistent with the previous studies [44,45]. The measured values for the Young's modulus E, Poisson's ratio υ, 0.2% proof strength $\sigma_{0.2}$, ultimate strength σ_u, strain at ultimate strength ε_u and fracture strain ε_f, are plotted against the build direction angle θ in Fig. 9. The results can be seen to be generally insensitive to loading direction, though the ultimate strength σ_u shows a clear increasing trend with increasing θ; this is consistent with previous findings [14,16,46].

3.2. Compressive coupon tests

Compressive coupon tests were conducted in an Instron 5984 150 kN universal testing machine, using the test setup shown in Fig. 10. Prior to testing, both coupon ends were machined to be flat and square, thereby ensuring uniform compressive loading during the tests. A random pattern of white speckles on a black background was applied on one side of each coupon and captured using a two-camera StrainMaster Portable DIC system, combined with LED lights, while an electrical resistance strain gauge was attached to the opposite side at mid-height to measure the longitudinal strains. The coupons were placed in a restraining jig

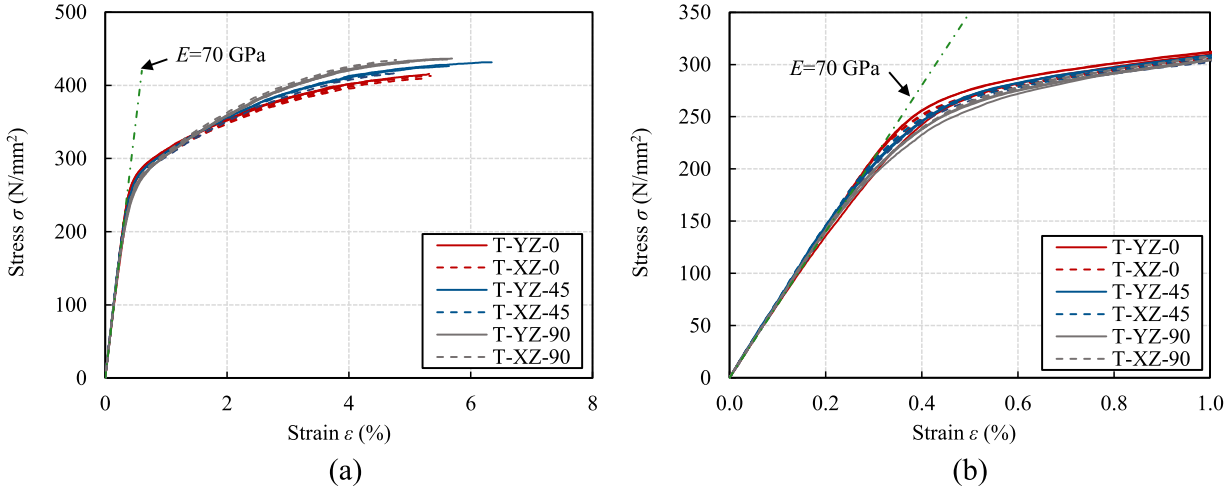

Fig. 6. Engineering stress-strain curves from tensile coupon tests over (a) the full range and (b) the initial range up to 1 % strain.

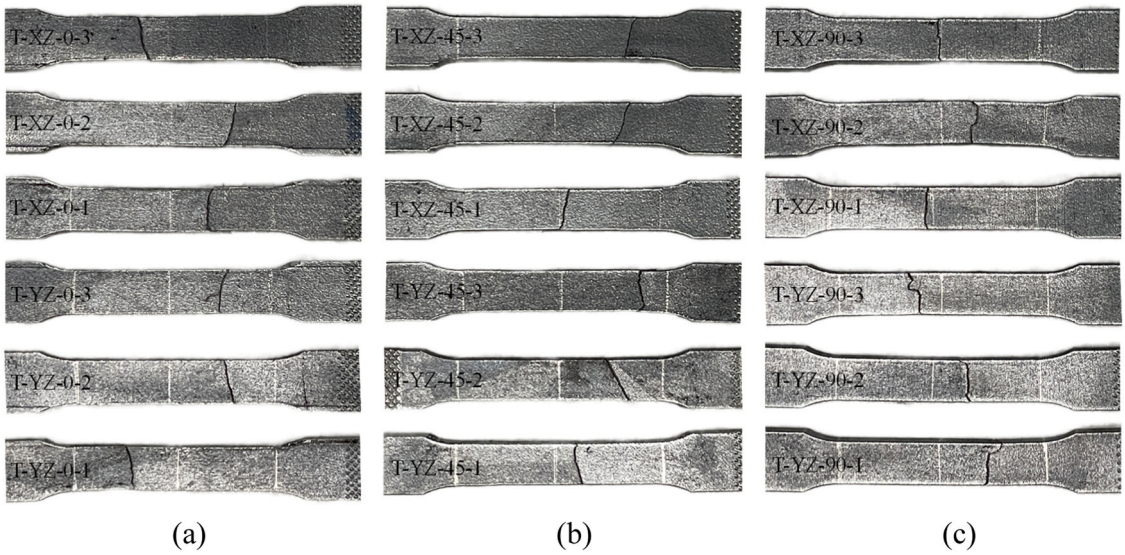

Fig. 8. Fractured coupons with (a) $\theta = 0^\circ$, (b) $\theta = 45^\circ$ and (c) $\theta = 90^\circ$.

Table 4
Key mechanical properties from tensile coupon tests.

Coupon ID	E (N/mm^2)	ν	$\sigma_{0.2}$ (N/mm^2)	$\sigma_{1.0}$ (N/mm^2)	$\sigma_{2.0}$ (N/mm^2)	σ_u (N/mm^2)	ε_u (%)	ε_f (%)	n	$m_{1.0}$	m_u
T-YZ-0-1	68800	0.34	283.1	332.7	369.7	415.5	5.3	5.7	7.8	1.9	2.2
T-YZ-0-2	71600	0.34	286.6	333.3	370.7	408.3	4.7	5.4	12.0	1.9	2.2
T-YZ-0-3	71900	0.33	286.4	333.1	370.5	398.4	3.8	4.3	12.5	1.8	2.0
T-XZ-0-1	72400	0.37	279.8	327.9	366.2	410.1	5.3	6.0	11.7	2.0	2.5
T-XZ-0-2	70400	0.33	279.0	329.1	367.8	413.7	5.3	6.1	10.3	1.9	2.4
T-XZ-0-3	71700	0.36	279.2	327.1	364.8	398.5	4.3	5.4	12.1	1.9	2.1
T-YZ-45-1	72800	0.31	281.2	332.9	374.6	432.7	6.3	7.1	7.5	1.8	2.3
T-YZ-45-2	72500	0.32	281.1	332.4	375.4	429.0	6.0	6.9	8.3	1.8	2.4
T-XZ-45-1	74000	0.32	276.1	329.4	373.4	416.6	4.6	5.1	8.8	1.7	2.1
T-XZ-45-2	70700	0.32	275.7	326.9	371.5	417.8	4.8	5.3	9.2	1.7	2.1
T-XZ-45-3	72700	0.34	279.0	331.2	375.4	420.9	4.7	5.1	9.5	1.7	2.1
T-YZ-90-1	71000	0.33	269.4	332.6	382.8	437.4	5.7	6.1	6.4	1.8	2.5
T-YZ-90-2	71800	0.34	272.6	331.1	380.9	432.2	5.1	5.9	7.0	1.7	2.1
T-YZ-90-3	72500	0.34	272.6	331.2	381.6	436.2	5.6	5.9	6.8	1.7	2.3
T-XZ-90-1	71500	0.34	275.9	336.5	386.4	436.2	4.8	5.1	6.7	1.7	2.1
T-XZ-90-2	71300	0.34	274.6	331.4	380.6	434.6	5.3	5.6	7.4	1.7	2.2
T-XZ-90-3	71300	0.34	276.8	333.7	383.6	433.2	4.6	5.0	7.1	1.6	1.9
Mean (0°)	71100	0.34	282.4	330.5	368.3	407.4	4.8	5.5	11.1	1.9	2.2
Mean (45°)	72500	0.32	278.6	330.6	374.1	423.4	5.3	5.9	8.7	1.7	2.2
Mean (90°)	71600	0.34	273.7	332.8	382.7	435.0	5.2	5.6	6.9	1.7	2.2
Mean (All)	71700	0.34	278.2	331.3	375.1	421.8	5.1	5.6	8.9	1.8	2.2
COV (All)	0.016	0.043	0.017	0.008	0.018	0.031	0.123	0.124	0.237	0.060	0.078

with the locking bolts finger tight to prevent premature minor axis buckling, while allowing expansion stemming from the Poisson's effect. The jig had a height of 70 mm, allowing the 75 mm × 16 mm coupons to protrude sufficiently beyond the jig ends, thereby enabling the application of compressive loads corresponding to strains of up to about 6 %. The coupon faces in contact with the jig were smeared with a thin layer of lubricating grease to reduce frictional effects. A similar setup has been successfully used in previous studies [47,48].

The compressive tests were carried out using displacement control at a constant rate of 0.075 mm/min up to 3 % compressive strain; this rate corresponded to that adopted in the stub column tests, as described in Section 5. Load and strain gauge readings were recorded using the DATASCAN acquisition system, while the transmitted load and DIC images were captured using the DaVis 10 software package [36], all of which were recorded at 1-second intervals.

The compressive stress-strain curves were determined, with the strains averaged from the strain gauge readings and longitudinal strains at mid-height derived from DIC, as shown in Fig. 11, where the typical value of $E = 70000$ MPa for conventional aluminium [39] is also plotted. The key mechanical properties obtained from the compressive coupon tests are summarised in Table 5, where the subscript 'c' denotes a compressive test. The compressive stress-strain characteristics of the examined PBF-LB/M aluminium were found to be influenced by the build direction, with the $\theta = 0^\circ$ coupons exhibiting the lowest 0.2 % proof strengths. Compared to the tensile properties described in subsection 3.1, the tested material had approximately 5 % higher Young's moduli and 1.0 % proof strengths.

4. Geometric measurements

The tested SHS stub columns had nominal cross-sectional dimensions (width B × height H × thickness t, as defined in Fig. 3(c)), of S50 × 50 × 4.0, S50 × 50 × 3.0, S50 × 50 × 2.5, S50 × 50 × 1.5, S50 × 50 × 1.2 and S50 × 50 × 1.0, with the letter 'S' denoting a stub

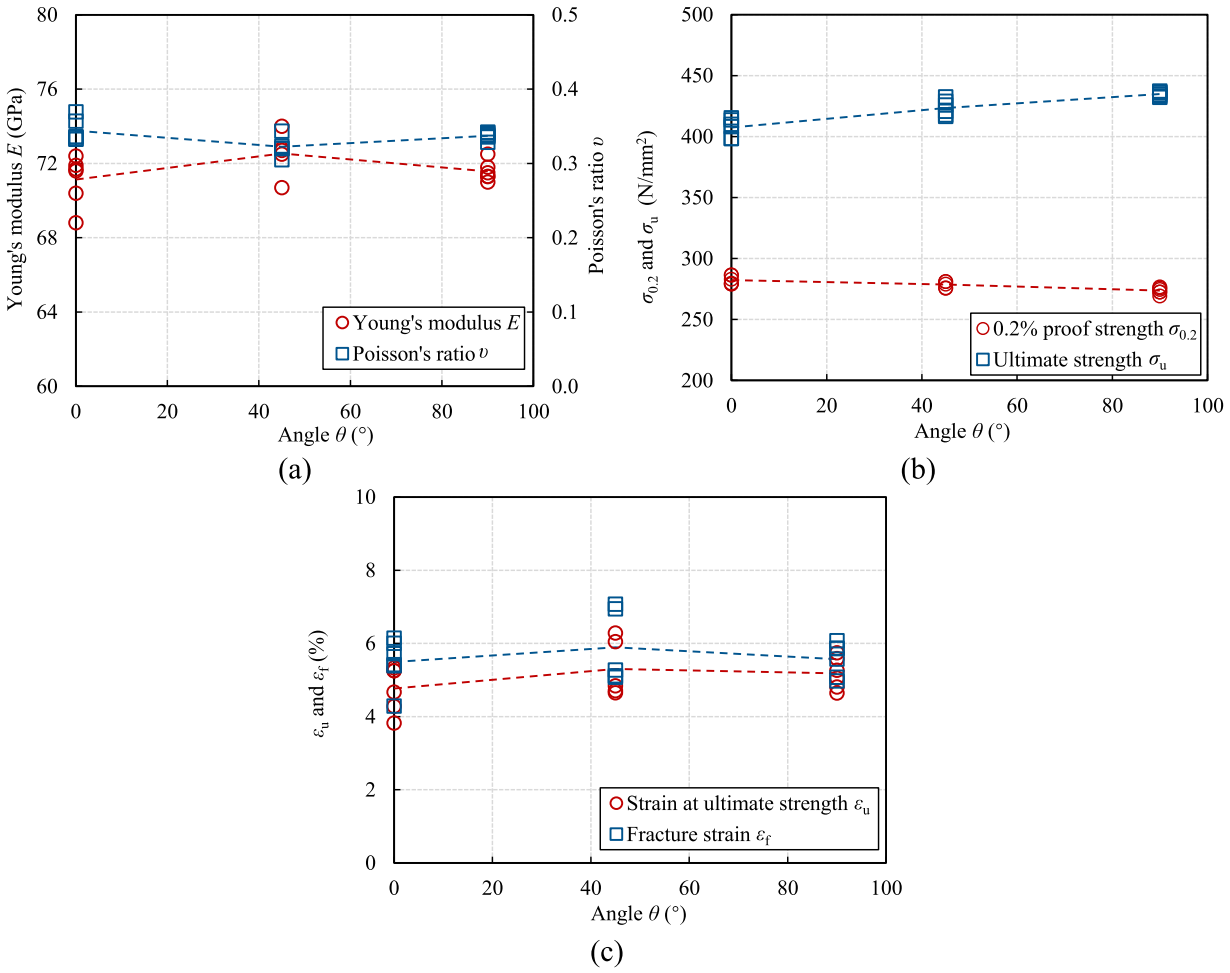

Fig. 9. Variation of (a) Young's moduli and Poisson's ratios, (b) 0.2 % proof and ultimate strengths and (c) strains at ultimate strengths and fracture strains with the build direction angle of PBF-LB/M aluminium coupons.

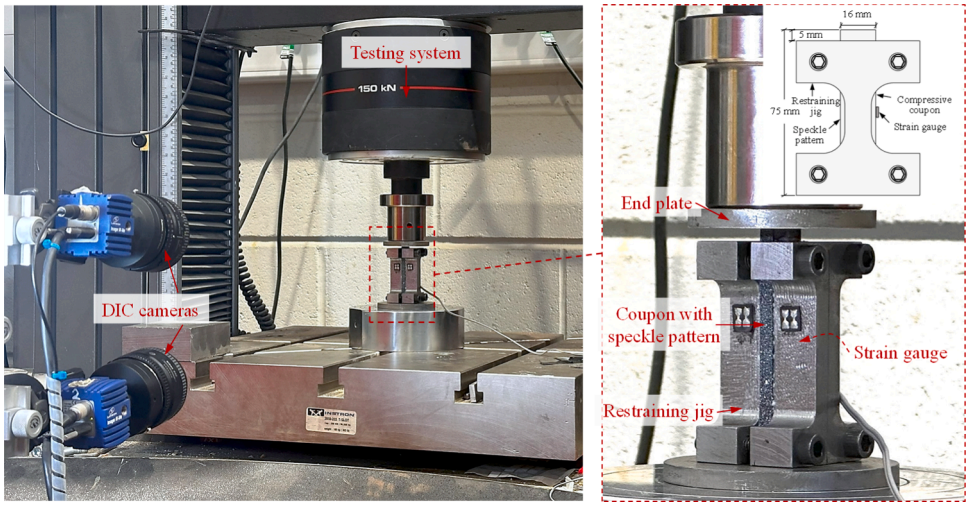

Fig. 10. Setup of compressive coupon tests, including schematic illustration of the restraining jig.

column, providing a range of cross-section slenderness values, covering Class 1 to Class 4. The nominal specimen length of the stub columns was set to 200 mm (i.e. four times the cross-section width), which was considered sufficiently long to include a representative pattern of local imperfections and residual stresses, yet short enough to preclude the effects of global buckling [49,50].

Prior to testing, the stub column ends were first machined flat and square to ensure a uniform distribution of compressive loading. The geometric properties of each specimen were determined through calliper and Archimedes' measurements, along with 3D laser scanning. Five measurements of the width B, height H and thickness t at both ends of each of the four individual sides of the cross-sections, along with the

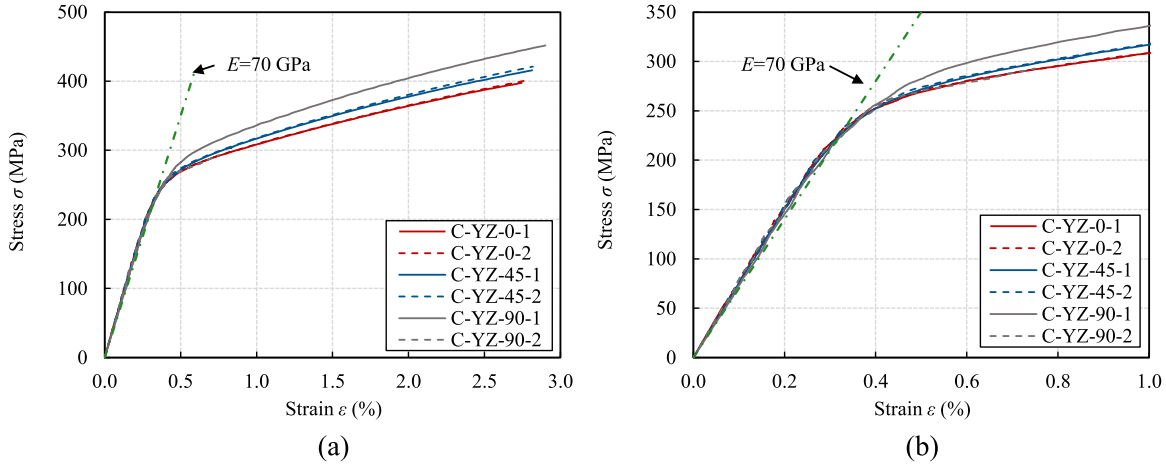

Fig. 11. Engineering stress-strain curves from compressive coupon tests.

Table 5
Key mechanical properties from compressive coupon tests.

Coupon ID	E_c (N/mm^2)	$\sigma_{0.2,c}$ (N/mm^2)	$\sigma_{1.0,c}$ (N/mm^2)	$\sigma_{2.0,c}$ (N/mm^2)	n	$m_{1.0}$	E_c/E	$\sigma_{0.2,c}/\sigma_{0.2}$	$\sigma_{1.0,c}/\sigma_{1.0}$	$\sigma_{2.0,c}/\sigma_{2.0}$
C-YZ-0-1	76500	275.6	334.7	387.9	10.3	1.5	1.08	0.98	1.01	1.05
C-YZ-0-2	74700	277.3	335.6	389.8	12.0	1.6	1.05	0.98	1.02	1.06
C-YZ-45-1	75400	281.0	347.1	403.8	9.7	1.7	1.04	1.01	1.05	1.08
C-YZ-45-2	77500	281.6	348.0	407.5	9.3	1.5	1.07	1.01	1.05	1.06
C-YZ-90-1	72400	300.4	373.8	437.5	9.1	1.6	1.01	1.10	1.12	1.14
C-YZ-90-2	77000	274.7	372.5	–	9.1	–	1.08	0.99	1.12	–
Mean (0°)	75600	276.4	335.2	388.8	11.1	1.6	1.06	0.98	1.01	1.06
Mean (45°)	76500	281.3	347.6	405.6	9.5	1.6	1.05	1.01	1.05	1.07
Mean (90°)	74700	287.5	373.1	437.5	9.1	1.6	1.04	1.04	1.12	1.14
Mean (All)	75600	281.8	352.0	405.3	9.9	1.6	1.05	1.01	1.06	1.08
COV (All)	0.025	0.034	0.049	0.049	0.113	0.052	0.026	0.045	0.045	0.034

overall length L, were taken using a digital calliper. The volume V and density ρ of each specimen were calculated using Eqs. (1) and (2), based on the measurements of their weights in air and in water (W_{air} and W_{water}) using a high-precision balance. An average density of 2.65 g/cm^3 was determined from the Archimedes' measurements, which is approximately equal to the value provided in the material data sheet (i.e. 2.67 g/cm^3). The cross-sectional area of each specimen, denoted as A_{Arch}, was calculated as the volume V divided by the measured length L, as presented in Table 6, where the cross-sectional area derived from the calliper measurements A_{cal} is also given for comparison.

$$V = \frac{W_{air} - W_{water}}{\rho_w g} \tag{1}$$

$$\rho = \frac{W_{air}}{gV} \tag{2}$$

To capture the out-of-flatness of the four faces of each specimen, a non-contact FARO ScanArm laser scanner with a reported accuracy of 0.1 mm and a minimum point spacing of 40 μm within its measurement range of 2.5 m [51], was employed to scan the external surface. The whole process for the determination of local imperfections from the raw scan data is shown in Fig. 12. The acquired point cloud data for each specimen were pre-processed in Geomagic Wrap [52], then imported into Rhino [53] in the form of a polygonal mesh. The model was aligned with the global coordinate system and contoured into cross-section slices along the specimen length, which were vertically sectioned into sets of longitudinal points along the flat constituent plates. The deviations from a linear trend line fitted to each set of longitudinal points were taken as the local geometric imperfections; a similar method for determining longitudinal imperfections using scan data has been reported in [9–11, 54]. Typical imperfection distributions for the most slender specimen, S50 × 50 × 1.0, are shown in Fig. 13, where outward and inward deviations are denoted as positive and negative, respectively. The maximum absolute deviation over the entire specimen was defined as the local imperfection amplitude of each specimen ω_{max}, as reported in Table 6. The local imperfection amplitudes were less than t/10 for all specimens, except for the most slender column S50 × 50 × 1.0.

Table 6
Measured dimensions and key test outputs of stub columns.

Specimen	B (mm)	H (mm)	t (mm)	L (mm)	A_{Hand} (mm^2)	A_{Arch} (mm^2)	ω_{max} (mm)	$N_{u,test}$ (kN)	$\delta_{u,test}$ (mm)	$N_{u,test}/N_{pl}$
S50 × 50 × 4.0	49.97	49.96	4.00	196.27	734.7	724.1	0.06	350.7	9.28	1.77
S50 × 50 × 3.0	50.00	49.98	3.02	197.68	566.6	551.0	0.07	233.9	5.40	1.55
S50 × 50 × 2.5	50.02	50.03	2.48	198.99	472.2	460.7	0.08	170.2	3.14	1.35
S50 × 50 × 1.5	50.03	50.05	1.45	199.38	282.2	276.8	0.09	56.5	0.62	0.75
S50 × 50 × 1.2	50.01	50.03	1.16	199.80	226.4	219.8	0.10	34.6	0.91	0.58
S50 × 50 × 1.0	50.02	50.02	0.95	199.78	186.8	180.7	0.13	23.5	1.08	0.47

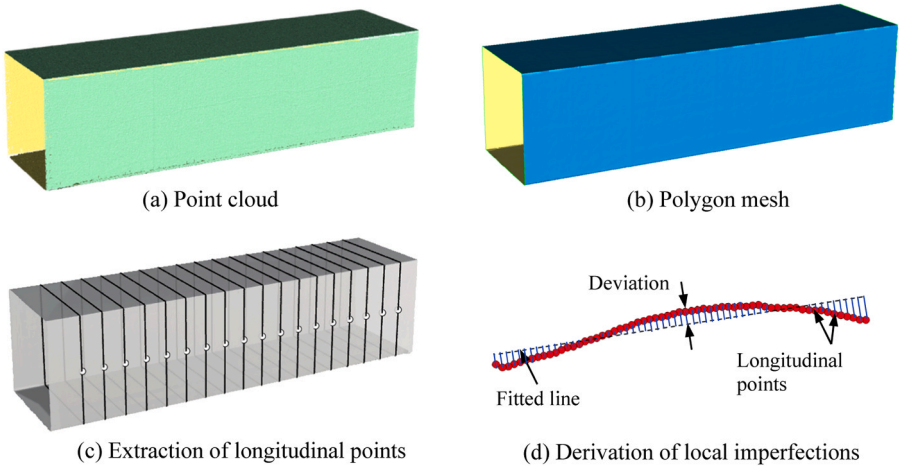

Fig. 12. Post-processing of scan data, showing the derivation of local imperfections.

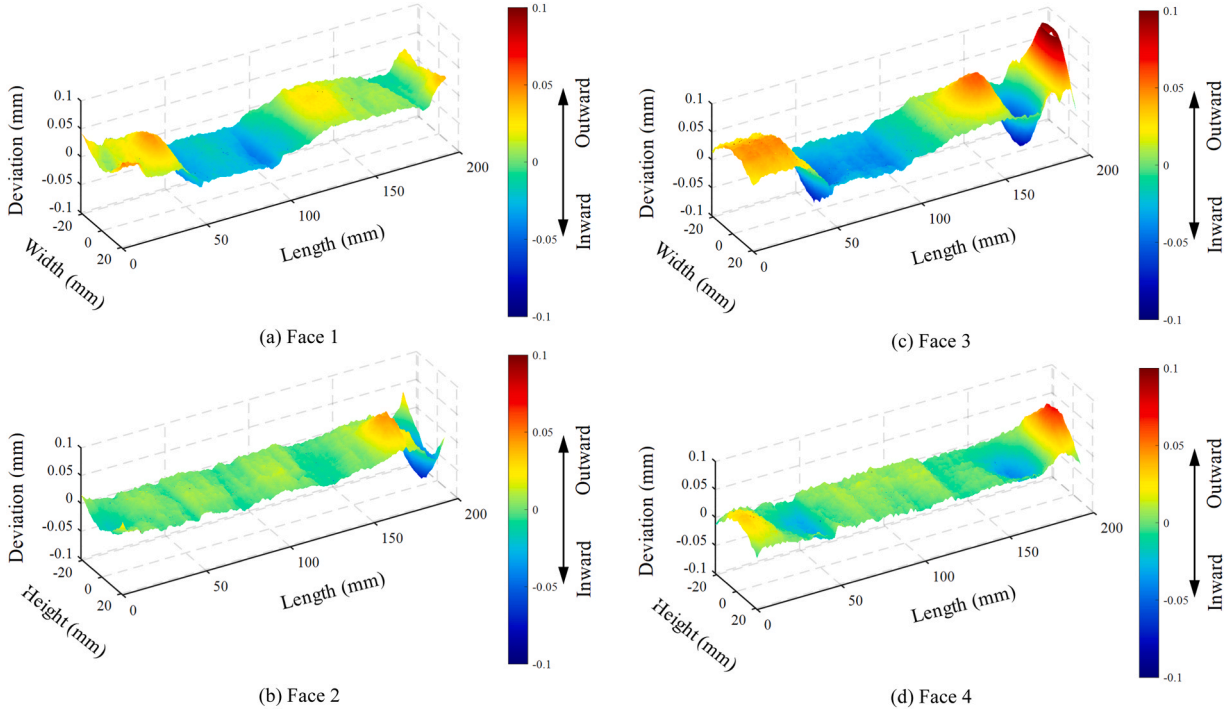

Fig. 13. Typical local imperfection distributions, shown for specimen S50 × 50 × 1.0.

5. Stub column tests

Six stub column tests were conducted to determine the cross-sectional behaviour of aluminium alloy SHS produced by PBF-LB/M. All tests were performed using an Instron 600 kN hydraulic testing machine, as shown in Fig. 14. The stub column specimens were positioned between a pair of hardened end plates to prevent damage to the testing machine from the high localised stresses, and a ball seating was used at the top end to compensate for any out-of-squareness of the specimen ends. The entire outer surface of each specimen was spray-painted with a matte black background and a random white speckle pattern of sizes larger than 4 pixels to create trackable features. Two stereo DIC systems, each consisting of two cameras and two LED illumination units, were employed to synchronously monitor the full-field strain and displacement data of the test specimens, following the recommendations set out in [28]. Each pair of DIC cameras was vertically oriented, and aligned to face the diagonals of the SHS specimens, as

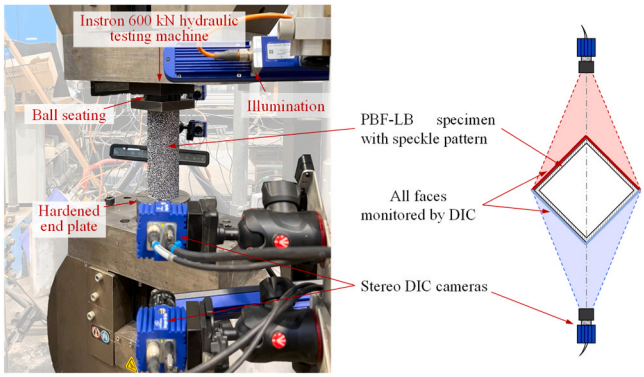

Fig. 14. Setup for stub column tests.

schematically shown in Fig. 14, enabling the acquisition of strains and deformations of all four faces of the SHS.

The stub column tests were conducted under displacement control at a compressive strain rate of approximately 0.1 % min^{-1}, and continued beyond the peak load to observe the initial unloading behaviour. The key outputs from the tests – the applied load, machine movement and DIC images, were captured at 1-second intervals using Davis 10 [36]. The post-processing and analysis of the DIC images were also performed using Davis 10 [36], with a subset size of 21 × 21 pixels, to contain at least 3 speckles in each subset, and a step size of 1/3 to 1/2 of the subset size, as recommended in [55].

The axial load-end shortening curve and DIC results, including the axial strain distributions and out-of-plane deformations, obtained from a typical stub column test – specimen S50 × 50 × 1.2, are shown in Fig. 15, where N is the applied load, and δ is the end shortening extracted using virtual extensometers in the DIC analysis. The specimen failed in the classical local plate buckling mode, with alternating inward and outward deformations between the cross-section faces [56]. All the axial load-end shortening curves obtained from the stub column tests are presented in Fig. 16. To enable direct comparisons between the stub column responses, the axial load-end shortening curves are plotted in a normalised form in Fig. 17, where $N_{pl}=A\sigma_{0.2}$ is the plastic load, with the cross-sectional area A taken as A_{Arch} and the 0.2 % proof strength $\sigma_{0.2}$ taken as the average value obtained from the tensile tests on the θ= 90° coupons, and $\delta_y=\sigma_{0.2}L/E$ is the theoretical end shortening at the plastic load. Overall, the initial slopes of all normalised load-end shortening curves align closely with the theoretical value, as represented by the black dashed line in Fig. 17. The ultimate loads $N_{u,test}$ and the

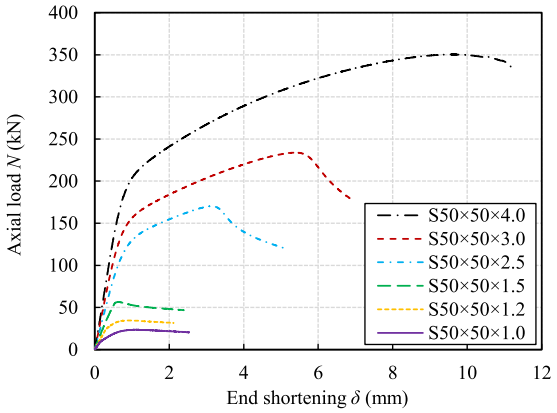

Fig. 16. Axial load-end shortening curves obtained from stub column tests.

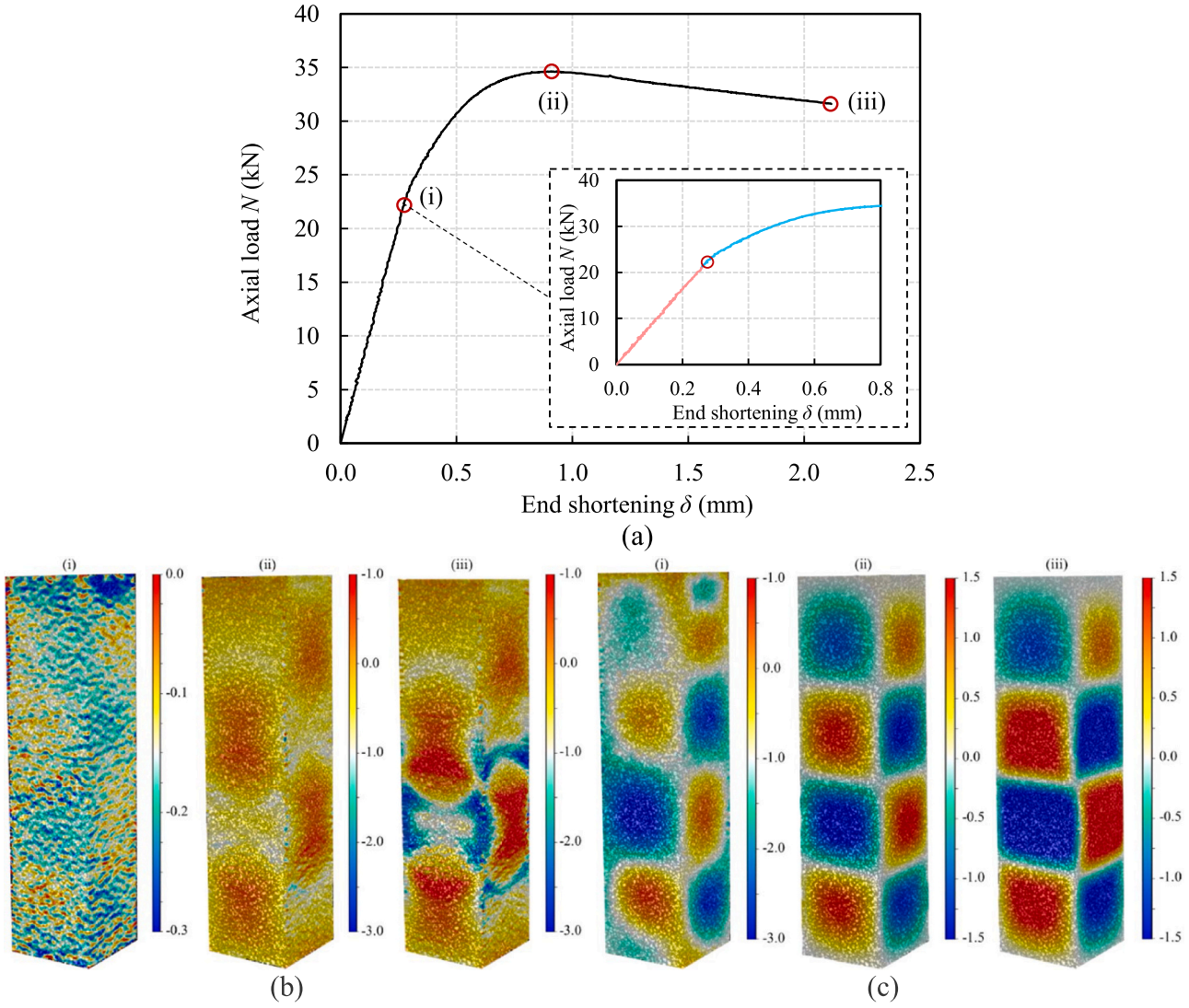

Fig. 15. (a) Axial load end-shortening curve for S50 × 50 × 1.2 and (b, c) corresponding DIC results, showing (b) axial strain distributions (unit: %) and (c) out-of-plane deformations (unit: mm) at (i) onset of stiffness reduction, (ii) just after N_u and (iii) on descending branch.

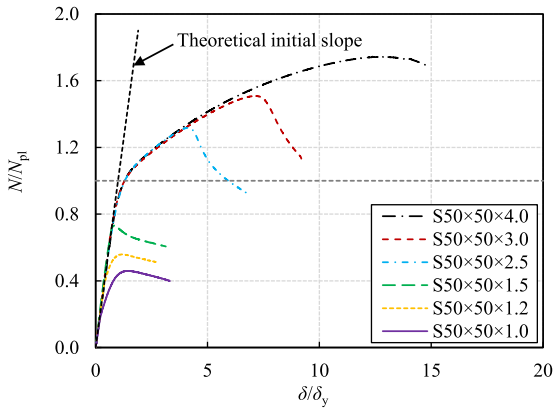

Fig. 17. Normalised axial load-end shortening curves obtained from stub column tests.

corresponding end shortening values $\delta_{u,test}$ are summarised in Table 6, along with the measured geometric dimensions. The tested stub columns exhibited the anticipated trend of reducing normalised capacity (i.e. lower $N_{u,test}/N_{pl}$ values) with increasing width-to-thickness ratio, highlighting the greater vulnerability to local buckling.

The deformed shapes of all specimens are presented in Fig. 18, and the post-ultimate out-of-plane deformations are also provided in Fig. 19 to quantitively visualise the failure modes, where outward and inward deformations are signified by positive (coloured in red) and negative (coloured in blue) values, respectively. The AlSi10Mg SHS stub columns manufactured by PBF-LB/M failed by inelastic local buckling, similar to equivalent conventionally manufactured aluminium SHS [57]. Local buckling was observed to be more pronounced in the more slender sections, as indicated by the lower normalised failure loads and the more pronounced out-of-plane deformations for specimens with $t = 1.0$ mm, 1.2 mm and 1.5 mm in Fig. 19. The delay of local buckling in the stockier sections enabled the specimens to deform into the strain hardening range, which led to the attainment of ultimate loads higher than the plastic load N_{pl} [58]. Note that the specimen S50 × 50 × 4.0 failed at an ultimate load greater than $A\sigma_u$, which is attributed to the increased cross-sectional area arising from the Poisson's effect in the compressed sections, and with a sudden crack near the bottom end on the descending branch.

6. Comparison with existing design methods

In this section, the applicability of two existing design methods for aluminium structures – EN 1999-1-1 [39] and the continuous strength method (CSM) [59–62] to the studied SHS produced by PBF-LB/M, is evaluated by comparing the experimental ultimate loads with the predicted cross-section resistances. Comparisons are also made against the available stub column test data on conventionally manufactured aluminium square and rectangular hollow sections (SHS and RHS). The average measured tensile material properties in the vertical ($\theta = 90°$) direction and the average measured geometric properties of the test specimens are utilised, with all partial safety factors for resistance set to unity. In total, 163 experimental data on aluminium hollow sections are considered, 6 of which were manufactured by PBF-LB/M (i.e. those tested herein) and 157 of which were conventionally manufactured [57, 63–73].

Fig. 18. Deformed PBF-LB/M SHS stub columns, with increasing wall thickness from left to right.

6.1. EN 1999-1-1

According to the European standard EN 1999-1-1 [39], aluminium cross-sections should first be classified as either non-slender (i.e. Class 1 to 3) or slender (i.e. Class 4) sections depending on the yield strength and the width-to-thickness ratios of the constituent plate elements. The resistance of non-slender cross-sections is set equal to the plastic load $A\sigma_{0.2}$, while for slender cross-sections, an effective cross-sectional area A_{eff} is adopted, determined by factoring down the thickness to account for local buckling. The local buckling reduction factor ρ_c is given by Eq. (3) and (4) for internal compression parts:

$$\rho_c = 1.0 \quad \text{for } \beta \le \beta_3 \tag{3}$$

$$\rho_c = \frac{C_1}{(\beta/\varepsilon)} - \frac{C_2}{(\beta/\varepsilon)^2} \text{ for } \beta > \beta_3 \tag{4}$$

where β/ε is the slenderness parameter, equal to $b/t\varepsilon$ with b=max (H, B)-2t and $\varepsilon = \sqrt{250/\sigma_{0.2}}$; the Class 3 limits β_3/ε are taken as 22, 20 and 18 for Class A, B and C internal compression parts, respectively. The examined aluminium material falls into Class C [39]. An alternative approach, provided in Annex H of EN 1999-1-1 [39], which utilises the stress σ_5 corresponding to a strain equal to five times the elastic strain $\varepsilon_y = \sigma_{0.2}/E$ for Class 1 cross-sections, was adopted for the comparisons made on the examined PBF-LB/M aluminium, with σ_5 taken as 358.5 MPa. For the collected test data, the ultimate strength σ_u for Class 1 cross-sections was used for the comparisons due to the unavailability of σ_5, with σ_u taken as $1.1\sigma_{0.2}$ – see Fig. 20.

The normalised ultimate loads N_u/N_{pl} are plotted against the slenderness parameter β/ε in Fig. 20, where the data have been separated into Class A (see Fig. 20(a)) and Class B and C (see Fig. 20(b)) and the corresponding EN 1999-1-1 design curves are also presented. Overall, the data points for the PBF-LB/M aluminium SHS stub columns generally align with the trend of the conventionally manufactured SHS and RHS data, while in the stocky range, the PBF-LB/M aluminium SHS data lie above the majority of the conventionally manufactured data, owing to the strong degree of strain hardening exhibited by the studied PBF-LB/M aluminium material. It can be seen from Fig. 20 that the current Class 3 limit is generally applicable to PBF-LB/M aluminium SHS. The experimental data of both the Class A and Class B material lie predominantly above the respective EN 1999-1-1 design curves, particularly in the low slenderness range due to the rather simplistic treatment of strain hardening. Note that these findings are made based on a limited number of test data, and further test data will be required to propose new slenderness limits and design buckling curves for compressed PBF-LB/M aluminium plated cross-sections.

The predicted ultimate loads based on EN 1999-1-1 and the continuous strength method, which is described in subsection 6.2, are compared with the PBF-LB/M stub column test results in Table 7. The ratios of the experimental ultimate loads N_u, including the test data for PBF-LB/M aluminium SHS and collected test data for conventionally manufactured aluminium SHS and RHS, to the resistance predictions according to EN 1999-1-1 $N_{u,EC9}$ are reported in Fig. 21 and Table 8. EN 1999-1-1 was observed to provide consistently safe-sided resistance predictions for both conventionally and PBF-LB/M additively manufactured aluminium plated cross-sections, as indicated by the mean value of $N_u/N_{u,EC9}$ being 1.06 with corresponding coefficient of variation (COV) of 0.13.

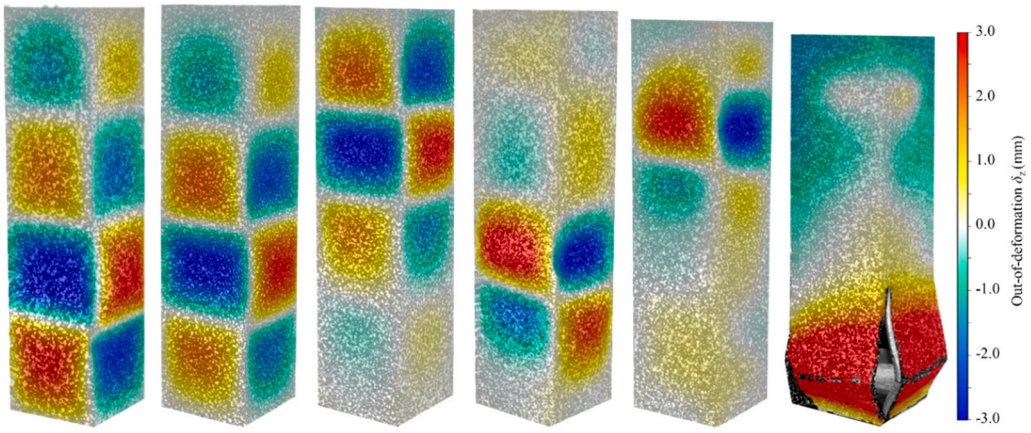

Fig. 19. Post-ultimate out-of-plane deformations of SHS stub columns, with increasing wall thickness from left to right.

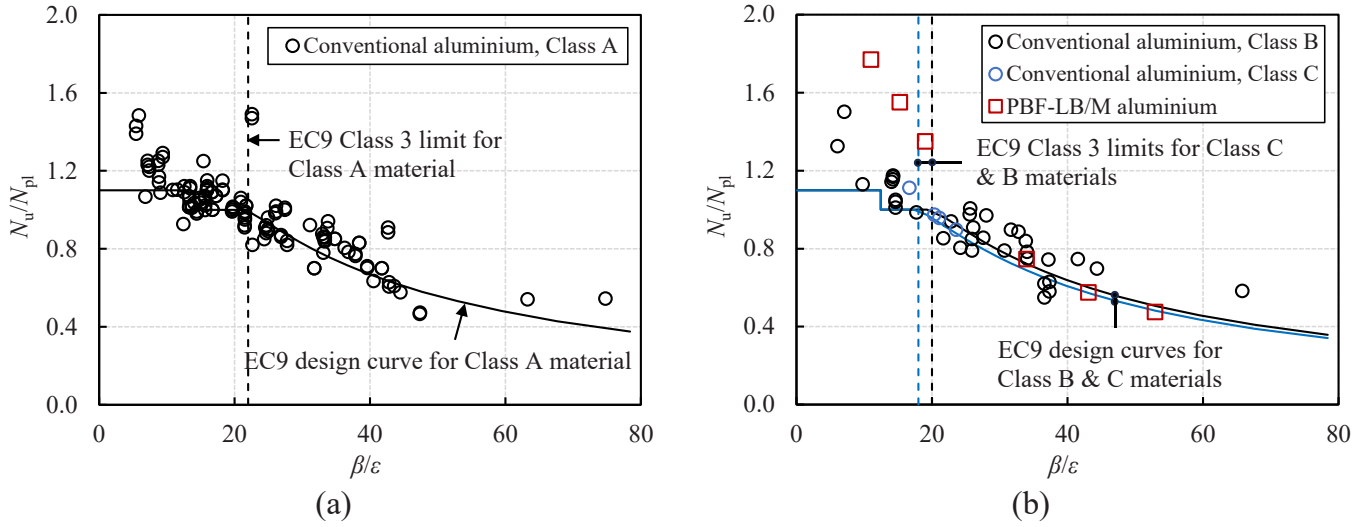

Fig. 20. Normalised ultimate axial resistance versus local slenderness and EC9 design curves for (a) Class A material and (b) Class B and C materials.

Table 7
Comparisons of stub column test results with EN 1999-1-1 and CSM resistance predictions.

Specimen	β/ε	EC9 Class	ρ_c	$N_{u,EC9}$ (kN)	$\bar{\lambda}_p$	$N_{u,csm}$ (kN)	$N_{u,test}/N_{u,EC9}$	$N_{u,test}/N_{u,csm}$
S50 × 50 × 4.0	11.0	1	1.00	263.4	0.38	315.0	1.33	1.11
S50 × 50 × 3.0	15.3	2	1.00	155.0	0.51	178.9	1.51	1.31
S50 × 50 × 2.5	19.0	4	0.98	126.6	0.62	130.7	1.34	1.30
S50 × 50 × 1.5	34.0	4	0.68	53.2	1.09	55.2	1.06	1.02
S50 × 50 × 1.2	43.1	4	0.57	35.4	1.37	36.3	0.98	0.95
S50 × 50 × 1.0	52.9	4	0.48	24.6	1.68	25.0	0.95	0.94

6.2. Continuous strength method (CSM)

The continuous strength method (CSM) method [74–77] features a base curve, defining the limiting failure strain ε_{csm} of a cross-section (i.e. its deformation capacity) as a function of the cross-sectional slenderness $\bar{\lambda}_p$, and a strain hardening material model and has been applied to plated [74–76,78] and circular hollow sections [59] made from structural carbon steel, stainless steel and aluminium. The CSM base curve is defined through the strain ratio $\varepsilon_{csm}/\varepsilon_y$, as expressed by Eqs. (5) and (6) for non-slender ($\bar{\lambda}_p \leqslant 0.68$) and slender ($\bar{\lambda}_p > 0.68$) plated cross-sections [57,59,60], respectively,

$$\frac{\varepsilon_{csm}}{\varepsilon_y} = \frac{0.25}{\bar{\lambda}_p^{3.6}} \leqslant \min\left(15, \frac{C_1\varepsilon_u}{\varepsilon_y}\right) \text{ for } \bar{\lambda}_p \leqslant 0.68 \quad (5)$$

$$\frac{\varepsilon_{csm}}{\varepsilon_y} = \left(1 - \frac{0.222}{\bar{\lambda}_p^{1.05}}\right)\frac{1}{\bar{\lambda}_p^{1.05}} \text{ for } 0.68 < \bar{\lambda}_p \leqslant 1.60 \quad (6)$$

where ε_{csm} is the maximum strain that a cross-section can endure before failure, ε_y is the yield strain equal to $\sigma_{0.2}/E$ with E being the Young's modulus, C_1 is a coefficient corresponding to the adopted CSM material model, which is taken as 0.5 for aluminium alloys, as recommended by Su et al. [57,60] and Yun et al. [43], ε_u is the strain at ultimate strength σ_u, and the cross-sectional slenderness is calculated by $\bar{\lambda}_p = \sqrt{\sigma_{0.2}/\sigma_{cr}}$,

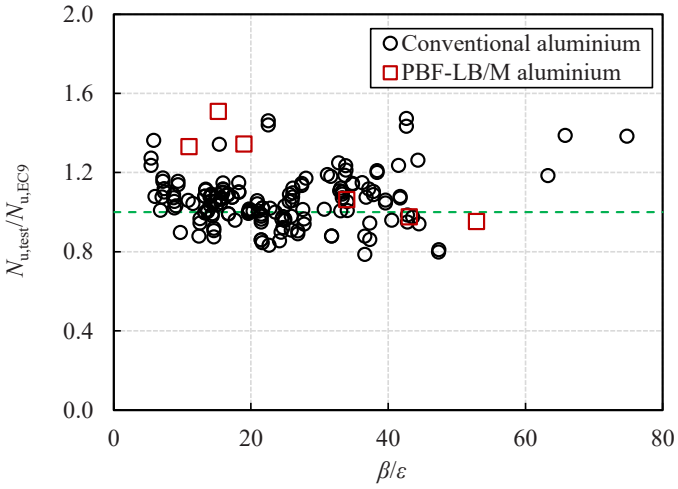

Fig. 21. Comparisons of experimental axial resistances with EN 1999-1-1 resistance predictions for aluminum SHS in compression.

Table 8
Comparisons of test results with EN 1999-1-1 and CSM compressive resistance predictions for PBF-LB/M and conventional aluminium SHS.

Manufacturing method	No. of data	Mean		COV	
		$N_{u,test}/N_{u,EC9}$	$N_{u,test}/N_{u,csm}$	$N_{u,test}/N_{u,EC9}$	$N_{u,test}/N_{u,csm}$
PBF-LB/M aluminum	6	1.20	1.11	0.19	0.14
Conventional aluminum [57,63–73]	157	1.06	1.04	0.12	0.12
All test data	163	1.06	1.04	0.13	0.12

with σ_{cr} being the elastic local buckling stress of the full cross-section, determined either using numerical tools, such as the finite strip software CUFSM [79] or approximate analytical formulae [80,81]. The experimental deformation capacity data $\varepsilon_{csm}/\varepsilon_y$ are plotted against the plate slenderness $\bar{\lambda}_p$, as presented in Fig. 22, together with the base curve expressed by Eqs. (5) and (6). The existing base curve for conventionally manufactured aluminum plated cross-sections can be seen to provide safe-sided predictions for aluminum cross-sections manufactured by PBF-LB/M.

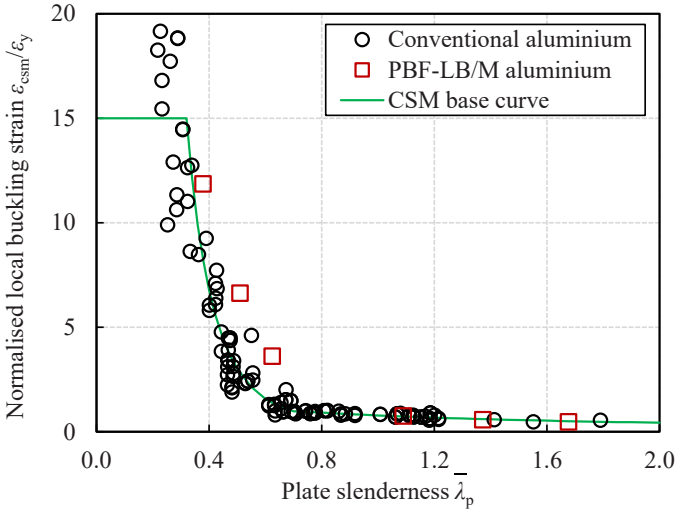

Fig. 22. Comparison between test results and the CSM base curve.

According to CSM, the compressive resistance of a plated cross-section is determined using

$$N_{csm} = \begin{cases} A\sigma_{csm} & \text{for} \quad \bar{\lambda}_p \le 0.68 \\ \dfrac{\varepsilon_{csm}}{\varepsilon_y} A\sigma_{0.2} & \text{for} \quad 0.68 < \bar{\lambda}_p \le 1.60, \end{cases} \tag{7}$$

where the bilinear constitutive model provided in [57,59] was adopted for aluminium alloys, as expressed by

$$\sigma_{csm} = \begin{cases} E\varepsilon_{csm} & \text{for } \varepsilon_{csm} < \varepsilon_y \\ \sigma_{0.2} + E_{sh}(\varepsilon_{csm} - \varepsilon_y) & \text{for } \varepsilon_y \le \varepsilon_{csm} \le C_2\varepsilon_u, \end{cases} \tag{8}$$

with the coefficient C_2= 0.5 and the strain hardening slope $E_{sh}=(\sigma_u - \sigma_{0.2})/(C_2\varepsilon_u - \varepsilon_y)$.

The experimental ultimate axial resistances normalised by the plastic load are plotted against the plate slenderness $\bar{\lambda}_p$ in Fig. 23, where the design curves for the PBF-LB/M AlSi10Mg and its conventional counterparts are also shown. The measured material properties in the vertical direction (θ=90°) were adopted for the PBF-LB/M AlSi10Mg specimens. The ratios of the experimental ultimate loads $N_{u,test}$ to the CSM resistance predictions $N_{u,csm}$ are reported in Fig. 24 and Table 8. The mean and COV values of $N_{u,test}/N_{u,csm}$ were 1.04 and 0.12, indicating that the resistance predictions obtained using the CSM are more accurate and less scattered than the EN 1999-1-1 predictions for both conventionally and additively manufactured aluminium plated cross-sections.

7. Conclusions

This paper presents an experimental study into the material and cross-sectional behaviour of additively manufactured aluminium square hollow sections (SHS). Six SHS stub columns, with a wide range of width-to-thickness ratios, were additively manufactured via laser beam powder bed fusion (PBF-LB/M) using AlSi10Mg powder feedstock and tested under axial compression, along with a series of as-built tensile and compressive coupons loaded at different angles relative to their build directions. Advanced measurement techniques – 3D laser scanning and digital image correlation, were employed for determining the geometric dimensions and deformations (and strains) of the test specimens.

The tested PBF-LB/M AlSi10Mg material exhibited good mechanical properties, and showed some mild anisotropy. The tested PBF-LB/M aluminium stub columns displayed the anticipated trend of reducing normalised load-carrying capacity with increasing plate slenderness owing to the increasing prominence of local buckling. Significant strain

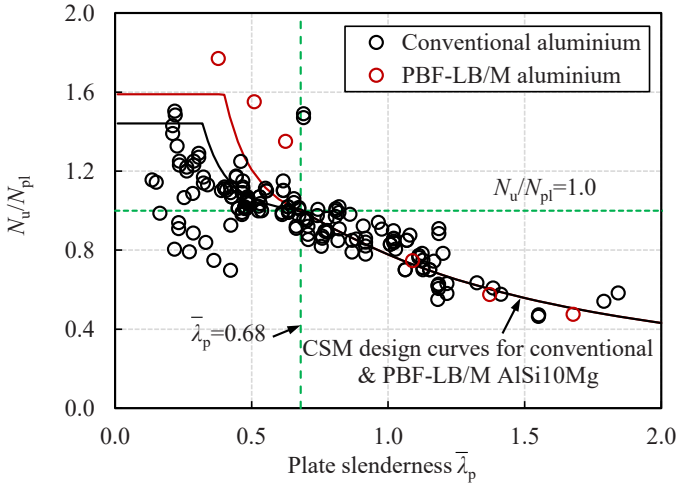

Fig. 23. Normalised ultimate axial resistance versus plate slenderness, showing CSM design curves for PBF-LB/M AlSi10Mg aluminium and conventional counterpart.

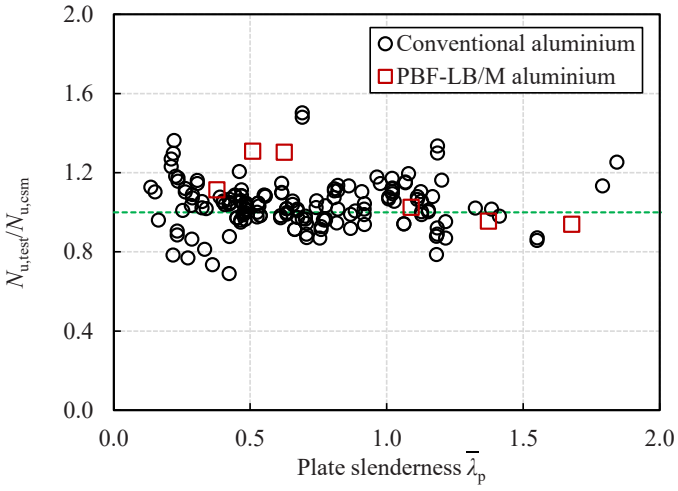

Fig. 24. Comparisons of experimental axial resistances with CSM resistance predictions for aluminum SHS in compression.

hardening was observed in the stocky cross-sections, while the stockiest cross-section exhibited brittle failure in the post-peak range.

The test results from the PBF-LB/M SHS stub columns were combined with additional test data on conventionally manufactured aluminium hollow sections collected from the literature and used to evaluate the accuracy of the resistance predictions obtained using EN 1999-1-1 and the continuous strength method (CSM). The comparisons indicated safe-sided resistance predictions for both design methods, with the CSM yielding more accurate and consistent results.

CRediT authorship contribution statement

Ruizhi Zhang: Writing – original draft, Visualization, Software, Methodology, Investigation, Formal analysis, Data curation, Conceptualization. **Heidi Piili:** Resources, Funding acquisition. **Mohsen Amraei:** Resources, Investigation. **Leroy Gardner:** Writing – review & editing, Supervision, Project administration, Methodology, Conceptualization.

Declaration of Competing Interest

The authors declare that they have no known competing financial interests or personal relationships that could have appeared to influence the work reported in this paper.

Acknowledgements

The authors would like to thank University of Turku for providing the test specimens and Krishna Choudhury, Paul Crudge and Freddy Olivo at Imperial College London for their assistance in the experimental programme.

Data availability

Data will be made available on request.

References

[1] Gardner L. Metal additive manufacturing in structural engineering – review, advances, opportunities and outlook. Structures 2023;47:2178–93.
[2] Meng X, Gardner L. Hybrid construction featuring wire arc additive manufacturing: review, concepts, challenges and opportunities. Eng Struct 2025;326:119337.
[3] Shah IH, Hadjipantelis N, Walter L, Myers RJ, Gardner L. Environmental life cycle assessment of wire arc additively manufactured steel structural components. J Clean Prod 2023;389:136071.
[4] Guo X, Kyvelou P, Ye J, Teh LH, Gardner L. Experimental investigation of wire arc additively manufactured steel single-lap shear bolted connections. ThinWalled Struct 2022;181:110029.
[5] Huang C, Li L, Pichler N, Ghafoori E, Susmel L, Gardner L. Fatigue testing and analysis of steel plates manufactured by wire-arc directed energy deposition. Addit Manuf 2023;73:103696.
[6] Zuo W, Chen M-T, Liu S-W, Yun X, Zhao O, Huang Y, et al. Experimental investigation on double-lap shear behavior of 3D printed austenitic stainless steel bolted connections. Eng Struct 2024;317:118501.
[7] Kyvelou P, Hong W, Zhang R, Gardner L. Mechanical properties and microstructure of wire laser metal deposited austenitic stainless steel. Mater Des 2025;250: 113558.
[8] Uzan NE, Shneck R, Yeheskel O, Frage N. High-temperature mechanical properties of AlSi10Mg specimens fabricated by additive manufacturing using selective laser melting technologies (AM-SLM). Addit Manuf 2018;24:257–63.
[9] Zhang R, Gardner L, Buchanan C, Matilainen VP, Piili H, Salminen A. Testing and analysis of additively manufactured stainless steel CHS in compression. ThinWalled Struct 2021;159:107270.
[10] Zhang R, Amraei M, Piili H, Gardner L. Microstructure, mechanical properties and cross-sectional behaviour of additively manufactured stainless steel cylindrical shells. ThinWalled Struct 2025;208:112750.
[11] Zhang R, Gardner L, Amraei M, Buchanan C, Piili H. Testing and analysis of additively manufactured stainless steel corrugated cylindrical shells in compression. J Eng Mech 2023;149:04023013.
[12] Khorasani A, Gibson I, Awan US, Ghaderi A. The effect of SLM process parameters on density, hardness, tensile strength and surface quality of Ti-6Al-4V. Addit Manuf 2019;25:176–86.
[13] Serjouei A, Libura T, Brodecki A, Radziejewska J, Broniszewska P, Pawłowski P, et al. Strength-hardness relationship for AlSi10Mg alloy produced by laser powder bed fusion: an experimental study. Materials Science Engineering A 2022;861: 144345.
[14] Read N, Wang W, Essa K, Attallah MM. Selective laser melting of AlSi10Mg alloy: process optimisation and mechanical properties development. Mater Des (19802015) 2015;65:417–24.
[15] Rosenthal I, Shneck R, Stern A. Heat treatment effect on the mechanical properties and fracture mechanism in AlSi10Mg fabricated by additive manufacturing selective laser melting process. Mater Sci Eng A 2018;729:310–22.
[16] Kempen K, Thijs L, Van Humbeeck J, Kruth J-P. Mechanical properties of AlSi10Mg produced by selective laser melting. Phys Procedia 2012;39:439–46.
[17] Costas M, Morin D, de Lucio M, Langseth M. Testing and simulation of additively manufactured AlSi10Mg components under quasi-static loading. Eur J Mech A/ Solids 2020;81:103966.
[18] Gite RE, Wakchaure VD. A review on process parameters, microstructure and mechanical properties of additively manufactured AlSi10Mg alloy. Mater Today Proc 2023;72:966–86.
[19] Weaver JS, Rosenthal I. Understanding anisotropic tensile properties of laser powder bed fusion additive metals: A detailed review of select examples. Gaithersburg, MD: US Department of Commerce, National Institute of Standards and Technology; 2021.
[20] Wang X, Muñiz-Lerma JA, Attarian Shandiz M, Sanchez-Mata O, Brochu M. Crystallographic-orientation-dependent tensile behaviours of stainless steel 316L fabricated by laser powder bed fusion. Materials Science Engineering A 2019;766: 138395.
[21] Meng X, Weber B, Nitawaki M, Gardner L. Optimisation and testing of wire arc additively manufactured steel stub columns. ThinWalled Struct 2023;189:110857.
[22] Weber B, Meng X, Zhang R, Nitawaki M, Sagawa T, Gardner L. Tensile behaviour of WAAM high strength steel material and members. Mater Des 2024;237:112517.
[23] Arrè L, Laghi V, Paola AM, Palermo M. Tubular sandwich cross-sections fabricated with wire Arc additive manufacturing for jumbo structural members. Structures 2024;67:106689.
[24] Laghi V, Palermo M, Gasparini G, Girelli VA, Trombetti T. Experimental results for structural design of Wire-and-Arc additive manufactured stainless steel members. J Constr Steel Res 2020;167:105858.
[25] Laghi V, Palermo M, Gasparini G, Trombetti T. Computational design and manufacturing of a half-scaled 3D-printed stainless steel diagrid column. Addit Manuf 2020;36:101505.
[26] Zhang R, Meng X, Gardner L. Shape optimisation of stainless steel corrugated cylindrical shells for additive manufacturing. Eng Struct 2022;270:114857.
[27] Ye J, Kyvelou P, Gilardi F, Lu H, Gilbert M, Gardner L. An end-to-end framework for the additive manufacture of optimized tubular structures. IEEE Access 2021;9: 165476–89.
[28] Meng X., Andy P., Guo X., Yun X., Gardner L. On the effective use of 3D laser scanning and DIC in structural testing. Journal of Constructional Steel Research [Submitted].
[29] Gardner L, Li J, Meng X, Huang C, Kyvelou P. I-section steel columns strengthened by wire arc additive manufacturing - concept and experiments. Eng Struct 2024; 306:117763.
[30] Hong W, Kyvelou P, Zhang R, Gardner L. Mechanical Testing and Microstructural Analysis of Wire Laser Beam Directed Energy Deposited Steel Plates. Materials & Design 2025:114141.
[31] SLM Solutions GmbH. Material Data Sheet of AlSi10Mg DIN EN 1706 / EN AC-43000. Lübeck, Germany: 2024.
[32] Kaufman JG. Properties of aluminum alloys: Tensile, creep, and fatigue data at high and low temperatures. ASM International; 1999.
[33] Kumar MS, Javidrad HR, Shanmugam R, Ramoni M, Adediran AA, Pruncu CI. Impact of print orientation on morphological and mechanical properties of L-PBF based AlSi7Mg parts for aerospace applications. Silicon 2022;14:7083–97.

[34] SMM Information & Technology Co., Ltd. Aluminum Alloy(A360) Price 2025. ⟨https://www.metal.com/Aluminum/202303030003⟩ (accessed February 20, 2025).
[35] CEN (European Committee for Standardization). Metallic materials - Tensile testing - Part 1: Method of test at room temperature. EN ISO 6892–1: 2019, Brussels, Belgium.
[36] LaVision Inc. Davis 10(2) 2021.
[37] Meng X, Gardner L. Behavior and design of normal-and high-strength steel SHS and RHS columns. J Struct Eng 2020;146(11):04020227.
[38] Meng X, Gardner L. Cross-sectional behaviour of cold-formed high strength steel circular hollow sections. ThinWalled Struct 2020;156:106822.
[39] CEN (European Committee for Standardization). Eurocode 9: Design of aluminium structures - Part 1-1: General structural rules. EN 1999-1-1:2023, 2023, Brussels, Belgium.
[40] Ramberg W., Osgood W.R. Description of Stress-Strain Curves by Three Parameters. National Advisory Committee for Aeronautics; 1973.
[41] Mirambell E, Real E. On the calculation of deflections in structural stainless steel beams: an experimental and numerical investigation. J Constr Steel Res 2000;54:109–33.
[42] Gardner L, Ashraf M. Structural design for non-linear metallic materials. Eng Struct 2006;28:926–34.
[43] Yun X, Wang Z, Gardner L. Full-range stress–strain curves for aluminum alloys. J Struct Eng 2021;147:04021060.
[44] Patakham U, Palasay A, Wila P, Tongsri R. MPB characteristics and Si morphologies on mechanical properties and fracture behavior of SLM AlSi10Mg. Materials Science Engineering A 2021;821:141602.
[45] Schuch M, Hahn T, Bleckmann M. The mechanical behavior and microstructure of additively manufactured AlSi10Mg for different material states and loading conditions. Mater Sci Eng A 2021;813:141134.
[46] Beretta S, Gargourimotlagh M, Foletti S, du Plessis A, Riccio M. Fatigue strength assessment of "as built" AlSi10Mg manufactured by SLM with different build orientations. Int J Fatigue 2020;139:105737.
[47] Foster ASJ, Gardner L. Ultimate behaviour of steel beams with discrete lateral restraints. ThinWalled Struct 2013;72:88–101.
[48] Yuan HX, Wang YQ, Shi YJ, Gardner L. Stub column tests on stainless steel built-up sections. ThinWalled Struct 2014;83:103–14.
[49] Ziemian R. Guide to stability design criteria for metal structures. Sixth edition. New York: John Wiley & Sons, Inc; 2010.
[50] Zhao O, Rossi B, Gardner L, Young B. Experimental and numerical studies of ferritic stainless steel tubular cross sections under combined compression and bending. J Struct Eng 2016;142:04015110.
[51] FARO. FARO 8-Axis Design ScanArm 2.0 2018.
[52] 3D Systems, Inc. Geomagic Wrap 2017.
[53] Robert McNeel & Associates. Rhino 7 2020.
[54] Meng X, Gardner L. Testing of hot-finished high strength steel SHS and RHS under combined compression and bending. ThinWalled Struct 2020;148:106262.
[55] Shin W, Yoo C. Application of the digital image correlation technique in wide width tensile test of geogrids. Geotext Geomembr 2024;52:1087–98.
[56] Zhao O, Gardner L, Young B. Buckling of ferritic stainless steel members under combined axial compression and bending. J Constr Steel Res 2016;117:35–48.
[57] Su M-N, Young B, Gardner L. Testing and design of aluminum alloy cross sections in compression. J Struct Eng 2014;140:04014047.
[58] Bock M, Gardner L, Real E. Material and local buckling response of ferritic stainless steel sections. ThinWalled Struct 2015;89:131–41.
[59] Gardner L, Yun X, Walport F. The continuous strength method – review and outlook. Eng Struct 2023;275:114924.
[60] Su M-N, Young B, Gardner L. The continuous strength method for the design of aluminium alloy structural elements. Eng Struct 2016;122:338–48.
[61] Gardner L, Nethercot DA. Structural stainless steel design: a new approach. Structural. Engineer 2004;82:21–30.
[62] Zhao O, Gardner L, Young B. Behaviour and design of stainless steel SHS and RHS beam-columns. ThinWalled Struct 2016;106:330–45.
[63] Han Q, Li M, Wang Z. Testing of high strength aluminium alloy SHS and RHS stub columns in fire. Eng Struct 2023;284:115971.
[64] Zhou F, Young B. Tests of concrete-filled aluminum stub columns. ThinWalled Struct 2008;46:573–83.
[65] Feng R, Young B. Experimental investigation of aluminum alloy stub columns with circular openings. J Struct Eng 2015;141:04015031.
[66] Zhi X, Wang Y, Li B, Zhang Y, Ouyang Y. Axial compression behaviour of 7A04-T6 high-strength aluminium alloy SHS and RHS stub columns. ThinWalled Struct 2022;180:109816.
[67] Faella C, Mazzolani FM, Piluso V, Rizzano G. Local buckling of aluminum members: testing and classification. J Struct Eng 2000;126:353–60.
[68] Langseth M, Hopperstad OS. Local buckling of square thin-walled aluminium extrusions. ThinWalled Struct 1997;27:117–26.
[69] Zhu J-H, Young B. Tests and design of aluminum alloy compression members. J Struct Eng 2006;132:1096–107.
[70] Piluso V, Pisapia A. Experimental and analytical study of SHS aluminium members under uniform compression. Eng Proc 2023;43:39.
[71] Mennink J. Cross-sectional stability of aluminium extrusions: prediction of the actual local buckling behaviour. PhD thesis, Technische Universiteit Eindhoven, 2002.
[72] Hassinen P. Compression strength of aluminium columns-experimental and numerical Studies. Couple Instab Met Struct CIMS'2000 2000:241–8.
[73] Bijlaard PP, Fisher GP. Column strength of H-sections and square tubes in postbuckling range of component plates. No. NACA-TN-2994. Washington: Cornell University; 1953.
[74] Yun X, Gardner L, Boissonnade N. The continuous strength method for the design of hot-rolled steel cross-sections. Eng Struct 2018;157:179–91.
[75] Ashraf M, Gardner L, Nethercot DA. Structural stainless steel design: resistance based on deformation capacity. J Struct Eng 2008;134:402–11.
[76] Liew A, Gardner L. Ultimate capacity of structural steel cross-sections under compression, bending and combined loading. Structures 2015;1:2–11.
[77] Gardner L, Yun X, Fieber A, Macorini L. Steel design by advanced analysis: material modeling and strain limits. Engineering 2019;5:243–9.
[78] Li P, Chen G, Qiu J, Qian J, Ding D, Jian B, et al. Experimental and numerical investigation into the load-carrying capacity of aluminium alloy H-sectional stocky columns under axial compression. J Build Eng 2024;87:108777.
[79] Li Z, Schafer BW. Buckling analysis of cold-formed steel members with general boundary conditions using CUFSM conventional and constrained finite strip methods (St. Louis, MO). Proceedings of the 20th international specification conference on cold-formed steel structures. 2010. p. 17–31 (St. Louis, MO).
[80] Gardner L, Fieber A, Macorini L. Formulae for calculating elastic local buckling stresses of full structural cross-sections. Structures 2019;17:2–20.
[81] Seif M, Schafer BW. Local buckling of structural steel shapes. J Constr Steel Res 2010;66:1232–47.